Joule

Article

Systematic feature design for cycle life prediction of lithium-ion batteries during formation

Graphical abstract

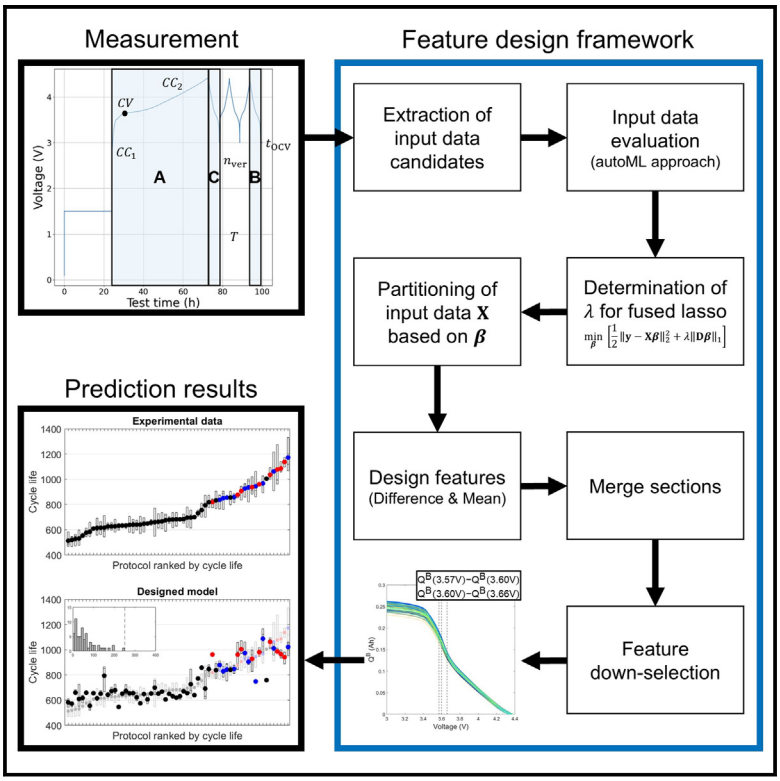

Highlights

- Systematic feature-design framework enables cycle life prediction during formation
- Interplay of data-driven feature design and mechanistic understanding is demonstrated
- Designed features capture temperature effect and particle-resistance heterogeneity
- Open-source software is provided that implements the feature-design framework

Authors

Jinwook Rhyu, Joachim Schaeffer, Michael L. Li, Xiao Cui, William C. Chueh, Martin Z. Bazant, Richard D. Braatz

Correspondence

braatz@mit.edu

In brief

We propose a systematic feature-design framework that allows the prediction of the cycle life of lithium-ion batteries within 10% error during the formation step. By reducing the evaluation time for formation protocols while requiring minimal domain knowledge, our work accelerates the optimization of formation steps. Our approach, which leverages the interplay between the data-driven feature design and mechanistic understanding, can be applied to other regression or classification problems in which limited domain knowledge is available.

Rhyu et al., 2025, Joule 9, 101884
May 21, 2025
https://doi.org/10.1016/j.joule.2025.101884

CellPress

Joule

CellPress

Article

Systematic feature design for cycle life prediction of lithium-ion batteries during formation

Jinwook Rhyu,[1] Joachim Schaeffer,[1,2] Michael L. Li,[1] Xiao Cui,[3,4] William C. Chueh,[3,4,5] Martin Z. Bazant,[1,6] and Richard D. Braatz[1,7,*]

[1]Department of Chemical Engineering, Massachusetts Institute of Technology, Cambridge, MA 02139, USA
[2]Control and Cyber-Physical Systems Laboratory, Technical University of Darmstadt, 64283 Darmstadt, Germany
[3]Department of Materials Science and Engineering, Stanford University, Stanford, CA 94305, USA
[4]Applied Energy Division, SLAC National Accelerator Laboratory, Menlo Park, CA 94025, USA
[5]Department of Energy Science and Engineering, Stanford University, Stanford, CA 94305, USA
[6]Department of Mathematics, Massachusetts Institute of Technology, Cambridge, MA 02139, USA
[7]Lead contact
*Correspondence: braatz@mit.edu
https://doi.org/10.1016/j.joule.2025.101884

SUMMARY

Optimization of the formation step in lithium-ion battery manufacturing is challenging due to limited physical understanding of solid-electrolyte interphase formation and the long testing time (~100 days) for cells to reach the end of life. We propose a systematic feature-design framework that requires minimal domain knowledge for accurate cycle life prediction during formation. By only using two simple $Q(V)$ features designed from our framework, extracted from formation data without any additional diagnostic cycles, we achieved an average of 9.87% error for cycle life prediction. The physics-based investigation guided by the two designed features shows that the voltage ranges identified by our framework capture the effects of formation temperature and microscopic-particle resistance heterogeneity. By designing highly predictive, robust, and interpretable features, our approach can accelerate industrial battery formation research, leveraging the interplay between data-driven feature design and mechanistic understanding.

INTRODUCTION

Accurate lifetime prediction of lithium-ion batteries accelerates battery optimization and improves safety.[1–4] Although this task is challenging due to complicated and convolved degradation mechanisms, various studies have demonstrated the potential in using data-driven approaches,[5–13] physics-based approaches,[14–18] and hybrid approaches.[19–26] For accurate battery-health monitoring, diagnostic techniques such as differential voltage fitting (DVF),[27–30] incremental capacity analysis (ICA),[31,32] electrochemical impedance spectroscopy (EIS),[10,33–35] and hybrid pulse power characterization (HPPC)[36,37] were developed for physics-based feature extraction during battery operation. Further optimization of these diagnostic techniques includes novel state of health (SoH) feature development[38–41] and diagnostic time reduction.[42,43]

Compared with the extensive research on lifetime prediction during operation, there have been few studies on lifetime prediction during the manufacturing process (i.e., *extreme* early cycle life prediction) because of the limited availability of public manufacturing data. In fact, the cycle life can vary greatly based on the protocol used during formation, in which a passivation layer of solid-electrolyte interphase (SEI) is rapidly formed on the anode to limit further degradation during use. For example, Weng et al.[44] showed that the nickel manganese cobalt (NMC)/graphite pouch cells with the fast-formation protocol proposed by Wood et al.[45] and An et al.[46] had on average ~25% longer cycle lives than the pouch cells with a baseline formation protocol when aging the cells in both room-temperature and high-temperature (45°C) cases. Recently, Cui et al.[47] showed that the cycle life can vary 2-fold by only manipulating the formation protocols. Moreover, the formation step is closely related to battery degradation and safety concerns,[48] highlighting the importance of optimizing formation.

Extreme early cycle life prediction using machine learning (ML) can accelerate the optimization of formation protocols and help build mechanistic understanding to the extent that features correlated with cycle life can be identified in the formation data. Weng et al.[44] proposed the low state-of-charge (SoC) resistance (R_{LS}) as a feature for extreme early cycle life prediction, achieving ~8% error[49] (~15% error for a dummy model) over the dataset composed of 40 cells with two different formation protocols using the single feature based on the strong linear correlation between R_{LS} and the cycle life. R_{LS} is not only predictive but also practical since it does not require additional equipment to be installed in the manufacturing process, unlike other characterization techniques such as EIS,[46,50,51] X-ray tomography,[52–54] or acoustic time of flight (ToF).[55,56] Furthermore, R_{LS}

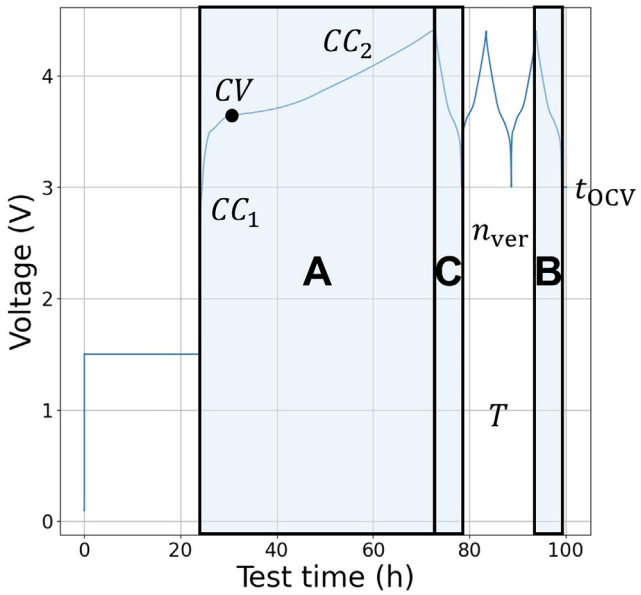

Figure 1. Schematic of formation protocols used for generating the dataset

A total of 62 protocols were tested by manipulating the six formation-protocol parameters: C-rate for the two-step charging (CC_1 and CC_2), the cutoff voltage between the two CC steps (CV), number of cycles between the first charge and last discharge step (n_{ver}), formation temperature (T), and the rest time (t_{OCV}). Three common steps among various formation protocols are indicated in blue: the first charge step (step A), the last discharge step (step B), and the first discharge step (step C). The figure is modified from Figure 1 in Cui et al.[47]

is easy to interpret since the feature is sensitive to lithium loss during formation.[44]

While R_{LS} is an interpretable, predictive, and an easy-to-implement feature, there are areas for further improvement. For example, the R_{LS} feature is highly sensitive to the SoC value where the resistance was measured, and thus its use requires accurate SoC estimation. According to Weng et al.,[44] the R_{LS} difference between the two formation protocols is roughly 10 mΩ (see Figure 3C in Weng et al.[44]). Given that the resistance varies roughly 75 mΩ with respect to 4% change in SoC at a low-SoC region (see Figure S9A in Weng et al.[44]), even a 0.5% error in SoC estimation can smear out the strong negative correlation between R_{LS} and the cycle life. Therefore, an additional low-rate cycle, which roughly takes a day to complete, is needed after the formation step to accurately calculate the full-cell SoC. Furthermore, R_{LS} only works for cells that undergo the same formation temperature (see Note S1). This fact indicates that a single R_{LS} feature is insufficient for optimizing formation, especially given that the formation temperature greatly impacts the cycle life.[47] These limitations motivate the development of new features that are (1) obtainable without additional diagnostic cycles and (2) capable of comparing formation protocols with different temperatures while still retaining the strengths of R_{LS}.

In this work, we propose a systematic framework to automatically *design* predictive yet interpretable features (i.e., transformation of input data) for regression problems. This framework is especially useful for investigating systems with complicated physics, such as SEI formation,[57] where automatic feature extraction can be more effective than handcrafted features that are limited by the many unknown aspects of the underlying physics. The performance of the *designed features* (i.e., the features designed from the proposed framework) for predicting the cycle life is then compared with agnostic and autoML approaches. Finally, we conduct a physics-based investigation, which is guided by the designed features, using a distributed-resistance model to explain the outstanding performance of the designed features.

METHODS

Description of the dataset

A dataset of 186 single crystal $Li[Ni_{0.5}Mn_{0.3}Co_{0.2}]O_2$ (SC-NMC532)/artificial graphite (AG) pouch cells with 62 different formation protocols (i.e., 3 cells per formation protocol) and an identical aging protocol, generated by Cui et al.,[47] was used in this study. The dataset includes 10 fast-formation protocols where both C-rates during the two-step charging step are greater than 1 C, which recently gained interest for improving the cell performance while reducing production costs.[44–47] Among the 186 pouch cells, we used 178 cells that reached the end of life (i.e., having a discharge capacity measured at 0.75 C constant current (CC) discharge step below 80% of its initial value measured at 0.75 C CC discharge step) without experimental failures such as shorting or broken tabs. Six parameters were varied in the dataset: the current for two-step CC at the first charge step (CC_1 and CC_2), the cutoff voltage between the two CC steps (CV), the number of cycles between the first charge and last discharge step (n_{ver}), the temperature during the formation step (T), and the rest time after the formation step (t_{OCV}). The six parameters were chosen using Latin hypercube sampling (LHS) for its ability to explore the parameter space efficiently.[58] Detailed data interrogation results using the six formation-protocol parameters and cycle life can be found in Note S2. We define three common steps that appear in all 62 formation protocols (see Figure 1): the first charge step (step A), the last discharge step (step B), and the first discharge step (step C). Most variations among the formation protocols are encoded in step A whereas steps B and C undergo the identical operating protocol at each T.

As a preliminary analysis, we constructed physics-*agnostic* ML models that map the six formation-protocol parameters to the cycle life. While the agnostic models cannot capture cell-to-cell variability (i.e., the variability between the cells that undergo the same protocol), they serve as a good baseline for evaluating model performance since the features directly encode the formation protocol. In this work, we used nested cross-validation to avoid information leakage,[59–62] with the detailed description provided in Note S3.

A total of 62 formation protocols were grouped into five sets, where one set was used as the test set and the remaining four as the training set in each outer fold to evaluate the model performance (see Figure S3). Within each outer fold, the inner loop was performed by dividing the training set into ten subsets, with one being used as the validation set and the others as the training set

Table 1. Hyperparameters of ML algorithms

ML algorithm	Hyperparameters	#
RR	L2 penalty term	1
EN	L1 penalty term, L2 penalty term	2
PLS	number of principal components (PCs)	1
SPLS	number of PCs, sparsity	2
RF	maximum depth of trees	1
SVR	regularization parameter, kernel coefficient, margin of tolerance	3
XGB	maximum depth of trees, L2 penalty term	2
ALVEN	degree, L1 penalty term, L2 penalty term	3
LCEN	degree, L1 penalty term, L2 penalty term	3

Table 2. Description of three categories for constructing agnostic models

Category description	Options	#
Formation protocol parameters	full set (CC_1, CC_2, CV, n_{ver}, T, t_{OCV})	2
	subset (CC_1, CC_2, CV, T)	
Log-transformed output	yes, no	2
ML algorithms	(linear) RR, EN, PLS, SPLS	13
	(nonlinear) RF, SVR, XGB	
	(nonlinear quantifiable) ALVEN, LCEN with degree of 1, 2, 3	

The subset of formation protocol parameters was selected based on shapley additive explanations (SHAP) analysis[73] conducted by Cui et al.[47]

in each inner fold for optimizing the hyperparameters listed in Table 1. A total of 52 agnostic models were constructed based on the combination of categories listed in Table 2. Smart process analytics (SPA) software[63] was used for model construction, which includes a suite of static ML algorithms: ridge regression (RR),[64] elastic net (EN),[65] partial least squares (PLS),[66] sparse partial least squares (SPLS),[67] random forest (RF),[68] support vector regression (SVR),[69] XGBoost (XGB),[70] algebraic learning via elastic net (ALVEN),[71] and lasso-clip-EN (LCEN).[72]

In this work, the *best* model is defined as the one with the smallest summation of the median and maximum mean absolute percentage error (MAPE) among the five outer folds to consider both average and extrapolation performances. Among the 52 agnostic models, the best model was the case with a subset of parameters, log-transformed output, and XGB algorithm (see Table 2), which had median and maximum MAPE of 11.06 and 11.35, and root mean square error (RMSE) of 107.10 and 124.81, respectively. Although the best agnostic model performs well, none of the agnostic models constructed in this study can be used for evaluating formation protocols that do not follow the (two CC charge step – n_{ver} CC charge/discharge cycles – CC discharge – t_{OCV} rest) template used by Cui et al.[47] This limitation arises because not all six formation-protocol parameters used in the agnostic models can be extracted from such protocols. Furthermore, the model cannot be used for diagnosing individual cell quality as it cannot capture the cell-to-cell variation.

Systematic feature-design framework

This section describes the workflow of the proposed systematic feature-design framework as displayed in Figure 2. We begin with extracting the input data (i.e., the source for designing features) candidates from the raw measurements. Then, the promisingness of each candidate is evaluated based on the autoML approach. After determining the promising input data types, we determine which value of penalty term λ to use for the fused-lasso model. Then, the features are designed based on the fused-lasso coefficient β that maps the selected input ($Q(V)$ in step B) to the output (cycle life). Last, the features are downselected to finalize the designed features.

Extraction of input data

The dataset contains seven measurements as a function of time (t) during the formation process: current (I), voltage (V), capacity (Q), energy (E), temperature (T), cycle index, and step index, where each measurement was taken at every 3 mV or 5 s for the CC step and at every 3 mA or 5 s for the constant voltage (CV) step, whichever comes first. Among various possible input data combinations, where the input variable (i.e., x in $f(x)$) and the function (i.e., f in $f(x)$) are selected from the measurements mentioned above, domain knowledge can be used to narrow down the most promising input data candidates. For example, the current I can be discarded because I is constant for most of the process. While t, V, and Q are monotonic functions within each step A, B, and C, and thus can be considered as input variables, the range for V is identical for all formation protocols whereas the range for t and Q within each step may vary from cell to cell. Therefore, the t and Q should be normalized when used as the input variable (i.e., $\tilde{t}, \tilde{Q} \in [0, 1]$). However, we may not use $\tilde{t}$ and $\tilde{Q}$ as input variables in step A since a single $\tilde{t}$ cannot specify the SoC of the cell whereas a single $\tilde{Q}$ masks the impact of C-rate, which greatly affects the electrode-utilization range,[47] given that the C-rates vary by orders of magnitude across different formation protocols in step A. In addition, any input data of $f(\tilde{t})$ and $f(\tilde{Q})$ are redundant for the CC steps due to $Q = It$, implying that only one may be considered for steps B and C. Thus, six input data types[74] are considered for the candidates: $Q^A(V)$, $t^A(V)$, $Q^B(V)$, $V^B(\tilde{t})$, $Q^C(V)$, and $V^C(\tilde{t})$.

Evaluation of input data

To design regression models with high prediction accuracy and robust generalization performance, we propose a method to select the input data that is *promising* for designing highly predictive features in this section. First, we construct *autoML* models using each input data candidate to evaluate their overall performance. Here, the autoML model refers to an ML model using features that are automatically extracted and selected without human assistance.[75] The tsfresh package,[76] which is a highly parallelized package recently used in lithium-ion battery applications[35,77,78] for extracting roughly 800 features from time-series data and guiding feature selection based on the feature importance,[79–81] was used in this step. From the features generated using tsfresh, we can construct a total of 2,448 autoML models based on the five categories listed in Table 3. For example, the autoML model with the first element in each category is constructed by first feeding $Q^A(V)$ to the tsfresh.extract_features

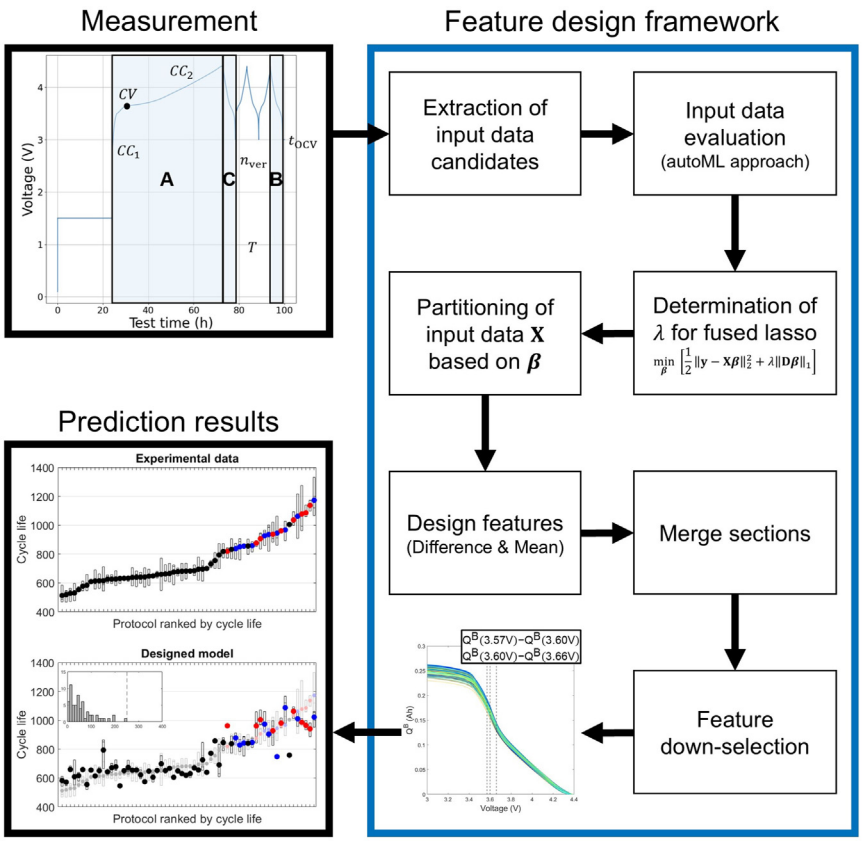

Figure 2. Systematic feature-design framework for extreme early cycle life prediction

The input to the framework is the measurements collected during the formation and the output is the two $Q^B(V)$ features where which (1) portion of the data to be used (e.g., steps A, B, or C), (2) data type to be used (e.g., $Q(V)$, $t(V)$, or $V(t)$), and (3) voltage or time values to be used for partitioning the input data are all systematically determined within the framework. The two $Q^B(V)$ features are used to evaluate the formation protocol during the formation step.

function, followed by pre-screening the features with p values larger than 10^0, followed by further feature selection using the tsfresh.select_features function with log-transformed cycle life. Then, these selected features are mapped onto the log-transformed cycle life using elastic net regression.

Similar to the evaluation of agnostic models, the median and the maximum of MAPE and RMSE among the outer folds were used as the performance metrics to evaluate each input data candidate (see Note S4). Given that we are constructing 408 autoML models for each input data type based on the combinations of categories listed in Table 3, where the number of features spans from one to more than hundreds, the input data type is not considered promising if none of the autoML models from the input data type outperform the best agnostic model in any of the four performance metrics.

The best autoML model with four input data types from steps B and C outperforms the best agnostic model in either MAPE or RMSE metrics, whereas the best model with two input data types from step A is strictly worse (see Figure S4). While this may seem counterintuitive as the features from step A directly encode the protocol-to-protocol variability and thus have more information than those from steps B and C, it can be explained by the discussion in Geslin et al.[61] According to Geslin et al.,[61] the features that encode operational variations (e.g., features from step A) are less capable of capturing cell-to-cell variability. This limitation arises because the predictive power of such features heavily depends on the characteristics of the protocols used for training. Therefore, the autoML models from step A would perform worse than the autoML models from steps B and C for predicting the cycle life of cells with untrained formation protocols (i.e., the extrapolation case; see the first row of Table 2 and the first panel of Figure S6 in Geslin et al.[61]). Note that the 62 formation protocols used in the dataset from Cui et al.[47] were designed using the LHS method over six formation-protocol parameters, indicating that the five outer folds in the nested cross-validation have a high level of extrapolation. Thus, the results in Figure S4 emphasize the importance of features that do not explicitly encode the operational variations for predicting the cycle life of the cells during formation for untrained formation protocols. While there are four input data types from steps B and C, we focus on $Q^B(V)$ in the subsequent parts since it showed the best performance in the MAPE metrics (see Note S9 for feature-design results with $V^B(\tilde{t})$, $Q^C(V)$, and $V^C(\tilde{t})$).

Determination of the linear-regression coefficient from input data

As an alternative to using nonlinear features, linear regression on high-dimensional data can also learn a nonlinear response.[82] One advantage of using linear-regression models is that we obtain a regression coefficient β that can give insights on how each portion of the input data contributes to the output estimation.[13,83] Among various linear models, we use the generalized lasso with penalty on the differences of adjacent coefficients (often referred to as fused-lasso[84]):

$$\min_{\beta \in \mathbb{R}^p} \frac{1}{2}\|\boldsymbol{y} - \boldsymbol{X}\boldsymbol{\beta}\|_2^2 + \lambda\|\boldsymbol{D}\boldsymbol{\beta}\|_1 \quad \text{with}$$

$$\mathbf{D} = \begin{bmatrix} -1 & 1 & 0 & \cdots & 0 \\ 0 & -1 & 1 & \ddots & \vdots \\ \vdots & \ddots & \ddots & \ddots & 0 \\ 0 & \cdots & 0 & -1 & 1 \end{bmatrix} \in \mathbb{R}^{(p-1)\times p}, \qquad \text{(Equation 1)}$$

to obtain regression coefficients β. Standardized input data $\boldsymbol{X}$ and output $\boldsymbol{y}$ are used when solving Equation 1 since the

Table 3. Description of five categories for constructing autoML models

Category description	Options	#
Input data types	$Q^A(V)$, $t^A(V)$, $Q^B(V)$, $V^B(\tilde{t})$, $Q^C(V)$, $V^C(\tilde{t})$	6
p values from univariate statistical test	10^0, $10^{-0.5}$, ⋯, $10^{-7.5}$, 10^{-8}	17
Further feature selection using tsfresh	yes, no	2
Log-transformed output	yes, no	2
ML algorithms	EN, RF, SVR, XGB, ALVEN, LCEN	6

The features extracted from the tsfresh package are first pre-screened based on the univariate statistical test (F-statistics) with the p value threshold chosen as in the second category. The features are further selected using select_features function in tsfresh package if the third category is "yes." The degree for ALVEN and LCEN was fixed to 1 as tsfresh package already contains various nonlinear transformations.

fused-lasso method uses a norm-based penalty term, where every column in $\boldsymbol{X}$ is divided by its maximum column-wise standard deviation (i.e., $\max_{j=1,\cdots,p}\mathrm{std}(\boldsymbol{X}_{:,j})$). Unlike standardizing each column of the input data, this method preserves the unique characteristic (e.g., trend of column-wise variance) of the raw data. This model yields sparsity in regression-coefficient difference (i.e., piecewise constant regression coefficients) roughly in line with physical expectations that neighboring regression coefficients should be similar and only change at specific locations. In turn, the fused-lasso regression coefficients can guide the partitioning of the input data into smaller sections and improve interpretability. Even from the same $\boldsymbol{X} \in \mathbb{R}^{n\times p}$ and $\boldsymbol{y} \in \mathbb{R}^{n\times 1}$, we can obtain various $\boldsymbol{\beta}$ by changing the penalty term λ. For example, having a larger λ would place a stronger penalty for $\boldsymbol{\beta}$ changing its values, making $\boldsymbol{\beta}$ *simpler* (see Figure S5D).

Considering the λ-dependency of $\boldsymbol{\beta}$, we should determine which value of λ leads to $\boldsymbol{\beta}$ for guiding the design of predictive yet interpretable features. For this process, we propose to determine λ based on three criteria: predictiveness, robustness, and interpretability. For predictiveness, the average of MAPE among five inner folds is used as the representative metric to evaluate how well the model predicts the cycle life of the cells with untrained formation protocols. The dynamic time warping (DTW) distance ratio metric[85,86] is used to quantify the robustness (i.e., how consistent the shape of $\boldsymbol{\beta}$ is for different training-test splits). Last, the average of path length along $\boldsymbol{\beta}$ among five inner folds is used for assessing the interpretability of $\boldsymbol{\beta}$. Details for determining λ can be found in Note S5. Then, the final $\boldsymbol{\beta}$ is obtained by solving Equation 1 with the determined λ.

Feature design based on β

In this step, we use the determined $\boldsymbol{\beta}$ as a template for designing predictive and interpretable features. The key advantage of using a linear model is that the regression problem can be split into smaller problems with a much simpler shape of $\boldsymbol{X}$ or $\boldsymbol{\beta}$ (i.e., $\hat{y} = \boldsymbol{X}\boldsymbol{\beta} = \sum_{m=1}^{M}\boldsymbol{X}_m\boldsymbol{\beta}_m$ where $\boldsymbol{X} = [\boldsymbol{X}_1, \cdots, \boldsymbol{X}_M]$ and $\boldsymbol{\beta} = [\boldsymbol{\beta}_1^T, \cdots, \boldsymbol{\beta}_M^T]^T$). Taking advantage of linearity, we can partition the input data into smaller sections based on the shape of $\boldsymbol{\beta}$, which makes $\boldsymbol{\beta}$ to be a flat line within each section. Figure 3A displays the standardized $Q^B(V)$ (Equation 2) of cells in the training set in colored solid lines and the determined $\boldsymbol{\beta}$ in black solid line for outer fold 1. The standardized $Q^B(V)$ of the i th cell is calculated as

$$\tilde{Q}_i^B(V_j) = \frac{Q_i^B(V_j) - \overline{Q}^B(V_j)}{\max \mathrm{std}\left(Q^B(V)\right)}, \qquad \text{(Equation 2)}$$

where $\overline{Q}^B$ is the column-wise average and $\mathrm{maxstd}(Q^B(V))$ is the maximum column-wise standard deviation of $Q^B(V)$ in the training set. The vertical dotted lines in Figure 3A indicate the boundaries for partitioning input data based on the indices where a jump (i.e., $|\boldsymbol{\beta}_{j+1} - \boldsymbol{\beta}_j| \geq 0.001 \times (\max \boldsymbol{\beta} - \min \boldsymbol{\beta})$) occurred.

Within each section partitioned by jumps in $\boldsymbol{\beta}$, it can be observed from Figure 3A that $\tilde{Q}_i^B(V)$ can be approximated into a line (e.g., $\tilde{Q}_i^B(V) = a_i V + b_i$). This linear approximation leads to the fact that only two features, the difference and the mean feature, are sufficient to represent each section. For example, such approximation leads to the relationship:

$$\begin{aligned}\hat{y}_i^{\text{section}}(V_1, V_2) :&= \sum_{j=\mathrm{ind}(V_1)}^{\mathrm{ind}(V_2)} \tilde{Q}_i^B(V_j)\boldsymbol{\beta}_j \approx \sum_{j=\mathrm{ind}(V_1)}^{\mathrm{ind}(V_2)} (a_i V_j + b_i)\boldsymbol{\beta}_j \\ &= a_i\left(\sum_{j=\mathrm{ind}(V_1)}^{\mathrm{ind}(V_2)} V_j\boldsymbol{\beta}_j\right) + b_i\left(\sum_{j=\mathrm{ind}(V_1)}^{\mathrm{ind}(V_2)} \boldsymbol{\beta}_j\right) \\ &= a_i C_1^y + b_i C_2^y,\end{aligned} \qquad \text{(Equation 3)}$$

where the ind function is for finding the index (i.e., $V_{\mathrm{ind}(V_j)} = V_j$), and C_1^y, C_2^y are constants. Here, the slope a_i can be expressed as

$$\begin{aligned}a_i &= \frac{\tilde{Q}_i^B(V_2) - \tilde{Q}_i^B(V_1)}{V_2 - V_1} \\ &= \frac{Q_i^B(V_2) - Q_i^B(V_1) + \overline{Q}^B(V_1) - \overline{Q}^B(V_2)}{(V_2 - V_1)\max \mathrm{std}\left(Q^B(V)\right)} \\ &= \left(Q_i^B(V_2) - Q_i^B(V_1)\right)C_1^a + C_2^a,\end{aligned} \qquad \text{(Equation 4)}$$

where C_1^a and C_2^a are constants. While various metrics can be used for representing the y-intercept b_i, we use $\mathrm{mean}(Q_i^B(V_1 - V_2))$ given that $\boldsymbol{\beta}$ is generally flat in each section. The value of b_i can be expressed as

$$b_i = \mathrm{mean}\left(Q_i^B(V_1 - V_2)\right)C_1^b + C_2^b, \qquad \text{(Equation 5)}$$

where C_1^b and C_2^b are constants. By combining Equations 3, 4, and 5, we conclude that only two features are needed to describe each section: $Q_i^B(V_2) - Q_i^B(V_1)$ and $\mathrm{mean}(Q_i^B(V_1 - V_2))$.

While there are 19 boundaries in Figure 3A, not all of the boundaries might be necessary for partitioning the input

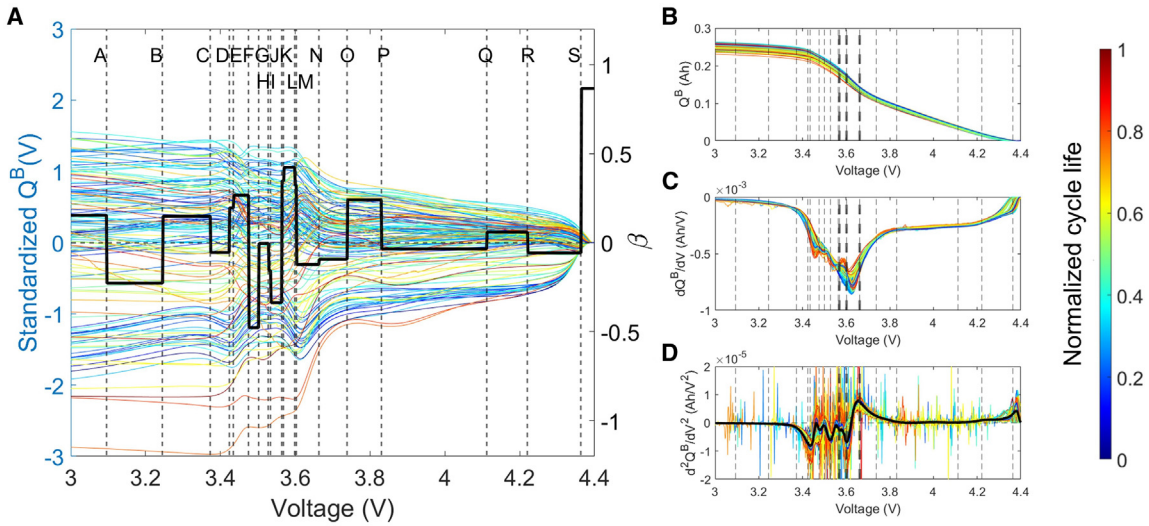

Figure 3. Input data partitioning for feature design

(A) Visualization of $Q_i^B(V)$ (colored solid lines) for all cells in the training set, β (solid black line), and partition boundaries where a jump occurred (vertical dotted lines) for outer fold 1 with $Q^B(V)$.

(B)–(D) (B) $Q^B(V)$, (C) $dQ^B/dV(V)$, and (D) $d^2Q^B/dV^2(V)$ with the vertical dotted lines indicating boundaries selected after Algorithm S1 (thin) and the three boundaries near 3.6 V selected after Algorithm S2 (thick). The colors indicate the normalized cycle life, and the thick black solid line in (D) is for the column-wise average. The color of curves at each panel indicates the normalized cycle life of the *i* th cell where 1 (red) is for the longest and 0 (blue) is for the shortest in the training set.

data. For example, boundaries L and M seem to be very close so that using only one might be sufficient. To determine whether we can remove the boundary $\text{ind}(V_j)$, we can check whether $\hat{y}_i^{\text{section}}(V_{j-1}, V_{j+1})$ can be well predicted with $Q_i^B(V_{j+1}) - Q_i^B(V_{j-1})$ and $\text{mean}(Q_i^B(V_{j-1} - V_{j+1}))$ (see Note S6 for the details). While boundary L is removed from Algorithm S1, we observe that neither boundaries J nor K can be removed although they seem to be very close to each other in Figure 3A. This highlights the fact that Algorithm S1 is actually sensitive to the information encoded in specific voltage ranges. In Figures 3B–3D, we plot the final partitioning obtained from Algorithm S1 on top of $Q^B(V)$, $dQ^B/dV(V)$, and $d^2Q^B/dV^2(V)$ graphs. From the figure, it is observed that the boundaries well capture the characteristics of $d^2Q^B/dV^2(V)$ curve, especially near the voltage range around 3.6 V where the largest peak and valley are identified (see thick vertical dotted lines in Figures 3B–3D).

When Algorithm S1 yields N^{sec} sections, we have $2N^{\text{sec}}$ features (difference and mean features in each section) in total. Among these, we can further down-select the features based on the correlation plot as shown in Algorithm S2 (see Note S7). First, we select the feature with the highest Pearson correlation with the cycle life. Then, the features that have a high Pearson correlation (e.g., >0.2) with the selected features are filtered out to avoid multicollinearity.[87–89] This process can be iterated until there is no feature left with a high Pearson correlation (e.g., >0.4) with the output. As a result, the two features, $Q^B(3.57\text{ V}) - Q^B(3.60\text{ V})$ and $Q^B(3.60\text{ V}) - Q^B(3.66\text{ V})$, were selected using Algorithm S2 for outer fold 1. The selected voltage values match with the index for the peak and valley of $d^2Q^B/dV^2(V)$ curve in Figure 3D, implying that the designed features capture some physical meaning.

The feature design results from other outer folds are displayed in Table 4 (see Note S8 for partitioning results in other outer folds). Consistency on the designed features among the outer loop (i.e., $Q^B(V)$ differences between ~ 3.57, ~ 3.60, and ~ 3.66 V) indicates the robustness of the feature design framework, which is remarkable given the high level of extrapolation at each outer fold since the 62 formation protocols used in Cui et al.[47] were designed using the LHS method.

RESULTS AND DISCUSSION

Evaluation of designed features

In this section, we evaluate the designed features by comparing the performance of the agnostic model, the autoML model, and the model trained by the designed features (i.e., *designed* model). A total of 13 designed models were constructed using the two features in Table 4 with 13 ML algorithms listed in Table 2. Table 5 displays the number of features, descriptions, and limitations of the best models (i.e., having the smallest sum of median and maximum MAPE among five outer folds) when using each approach. The mean, Hodges-Lehmann (HL) estimator,[90] median, and maximum for MAPE and RMSE metrics of the three models are visualized in Figure 4A. The model with small MAPE and RMSE metrics is placed at the lower-left corner of each panel in Figure 4A. The detailed values of each metric are given in Table 6.

From Figure 4A, we observe that the best designed model that uses only two features (blue star) has a performance comparable to the best autoML model (black cross), while outperforming the best agnostic model (red star) for mean, HL, and median metrics. This result is especially remarkable given that

Table 4. Feature design results for each outer fold when using $Q^B(V)$

Outer fold	Designed feature 1	Designed feature 2
1	$Q^B(3.57\ V) - Q^B(3.60\ V)$	$Q^B(3.60\ V) - Q^B(3.66\ V)$
2	$Q^B(3.58\ V) - Q^B(3.61\ V)$	$Q^B(3.61\ V) - Q^B(3.64\ V)$
3	$Q^B(3.57\ V) - Q^B(3.61\ V)$	$Q^B(3.61\ V) - Q^B(3.64\ V)$
4	$Q^B(3.58\ V) - Q^B(3.60\ V)$	$Q^B(3.60\ V) - Q^B(3.67\ V)$
5	$Q^B(3.57\ V) - Q^B(3.60\ V)$	$Q^B(3.60\ V) - Q^B(3.64\ V)$

Table 5. Description of the best agnostic, autoML, and designed models

Models	# Features	Description	Limitation
Agnostic (best)	4	subset (CC_1, CC_2, CV, T)/yes/XGB	limited to specific template no cell-to-cell variability
AutoML (best)	155	$Q^B(V)/10^{-4.5}$/yes/yes/SVR	nearly zero interpretability
Designed (best)	2	features in Table 4 with RF	–

See Tables 2 and 3 for details on the best agnostic and autoML models, respectively.

the designed features overcome the main limitations of other approaches; the agnostic model is limited to the specific format of formation protocols and cannot capture cell-to-cell variability, whereas the autoML model is the extreme case where the interpretability of the model is sacrificed to obtain a better predictive model. On the other hand, the designed model uses two simple $Q(V)$ features that can be applied to formation protocols that do not necessarily follow the template used by Cui et al.[47] These facts provide the designed model with both high flexibility and interpretability, which makes it appropriate for evaluating various innovative formation protocols during the formation step. Regarding the prediction errors of ~9%–10% MAPE, it should be noted that (1) the models here only use the measurements collected during the formation step, and (2) each outer fold has a high level of extrapolation since the formation protocols were designed by the LHS method.[47] In fact, the best achievable prediction error based on cell-to-cell variation is ~6% MAPE where the details are given in Note S10.

Figure 4B visualizes the actual and predicted cycle lives of the cells at each formation protocol, which indicates the accuracy and trustworthiness of the three models for evaluating untrained formation protocols. Predictions from the best agnostic model tend to have large deviations from the experimental data for the majority of formation protocols with long cycle life, which are mostly unconventional formation protocols including the fast-formation protocols and the high-temperature (i.e., T = 55°C) protocols. While the best autoML and designed models also have some protocols with large deviations, many of them have large variations within the predicted cycle lives (i.e., long error bar). These variations indicate that the evaluation of such formation protocols may not be trustworthy, and thus additional cell testing could lead to a better evaluation. The agnostic model cannot give such guidance to the user since it does not capture any cell-to-cell variability, implying the limitation of the agnostic model. The best autoML model shows a big prediction error (i.e., >250 cycles) in two fast-formation protocols, especially for the formation protocol with the longest cycle life where the prediction error is ~350 cycles. Thus, it can be risky to rely on autoML models to evaluate fast-formation protocols. The best designed model shows a prediction error of ~250 cycles for protocol 34, which has an average cycle life of ~1,000 while not being a fast-formation nor high-temperature protocol. However, it should be noted that the best autoML model also shows a prediction error of ~200 cycles for that protocol, and thus this poor prediction is likely due to the limitation of using only $Q^B(V)$ data for constructing the models. Overall, the best designed model shows a prediction error of fewer than 200 cycles for all fast-formation and high-temperature formation protocols while also capturing cell-to-cell variability, indicating a good trustworthiness for evaluating across a wide range of formation protocols.

We attribute the outstanding performance of the designed features to the fact that our partitioning algorithm well identifies specific voltage ranges with critical information (see Figure 3). The features generated from the autoML approach typically use either the entire dataset or subset of the dataset that is chosen based on simple statistics (e.g., percentile or arbitrarily chosen thresholds). On the other hand, the features designed from our framework use the subset that is determined by considering the relationship between the input data and the output (e.g., jumps occurred within β or Algorithm S1). Since the designed features use a subset of input data with similar information one at a time, they are sensitive to voltage-specific information, ultimately leading to a high predictive power.

Physical meaning of the designed features

From the domain knowledge (indicated as red arrows in Figure 5), we know that the formation temperature and the heterogeneity of microscopic-particle resistances are the main factors for the SEI quality, which ultimately impacts the cycle life. From the feature-design work above (indicated as blue arrows in Figure 5), we learned that the three voltage values that appear in the designed features in Table 4 match the peak and valley of the d^2Q/dV^2 curve at step B. In order to learn the physical meaning of the designed features, we investigate the missing link indicated as the dotted green line in Figure 5.

In this section, we investigate the impact of formation temperature and heterogeneity of microscopic-particle resistances on the dQ^B/dV and d^2Q^B/dV^2 curves at the formation step. From this, we aim to develop a foundational understanding of how the two features designed solely from the data-driven approach can be effective at predicting the cycle life of the cells from the unseen formation protocols. As shown in Figures 3B–3D, the designed features do not directly correspond to features in the dataset's average discharge capacity or differential capacitance curves, which have been widely used in previous studies as indicators of lifetime.[6,92–94] However, the voltage windows identified

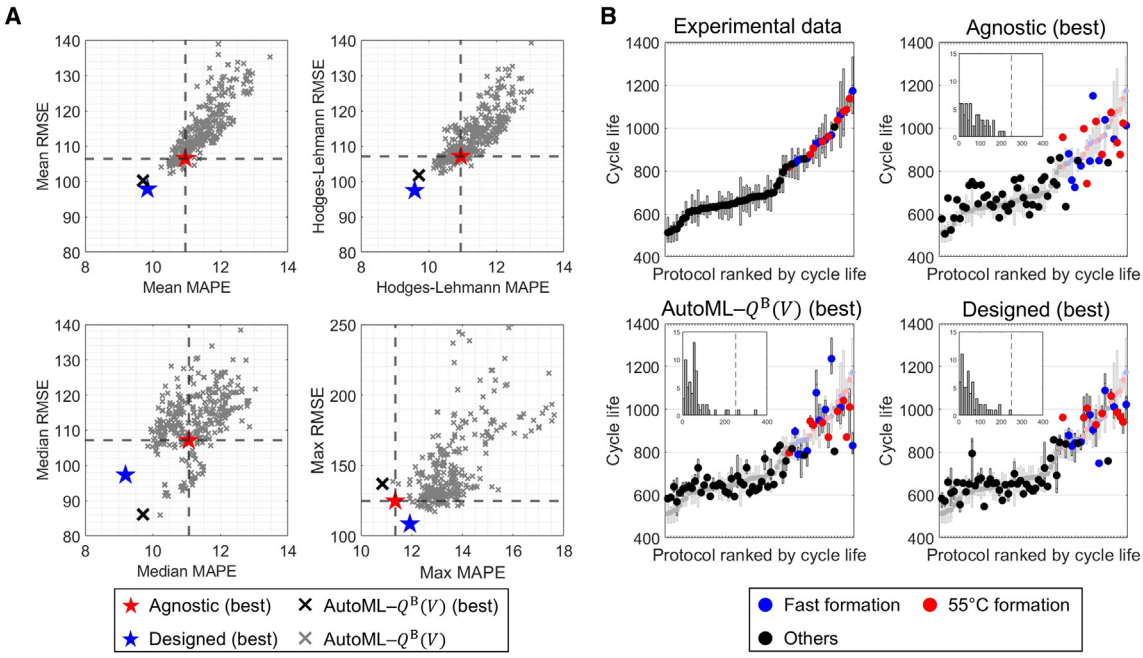

Figure 4. Predictive performance of the agnostic, autoML, and the designed models

(A) Scatter plots of mean, HL estimator, median, and maximum for MAPE and RMSE.

(B) Average (dot) and maximum and minimum (error bar) of true and predicted cycle lives per each formation protocol. The protocols are sorted by the average cycle life from the experimental data. The inset shows the histogram of prediction errors (i.e., the difference between the average of actual and predicted cycle lives) of all 62 formation protocols with the dotted vertical line marking 250.

from our framework show a strong overlap with local maxima and minima in the dataset's average second derivative of capacity (d^2Q/dV^2) data, particularly in the range of 3.4–3.7 V where the downselected features in Table 4 are concentrated. This alignment between key curve-defining features of the dataset, like the maxima and minima curvature regions, and the selected voltage points highlights the high interpretability of the designed features.

Given the wide variations in the formation protocols within the dataset, precisely interpreting the physical meaning of these features is challenging. Therefore, we explore the features specific to the slow formation, where CC_1 is below 0.05 C. These formation protocols are expected to be more predictable as long cycle life performance is physically tied to the formation of a stable SEI layer under these slow operating conditions. Furthermore, these stable SEI layers can be viewed as a fixed amount of lithium loss, which makes it easier to investigate by removing the degrees of freedom derived from the electrode-utilization shift. For slowly formed Li-ion battery systems, it has long been hypothesized that SEI growth is the dominant mechanism for capacity fade, which becomes self-limiting at long times due to the diffusion limitation of solvent molecules across the SEI layer.[45,57,95–100] A dynamical transition from reaction-limited to diffusion-limited SEI growth has also been proposed,[92] roughly corresponding to classical two-layer models of SEI growth, in which the rapid electrodeposition of a dense, inorganic primary SEI layer is followed by slow, diffusion-limited growth of a thick, porous secondary SEI layer.[99,101–103] Recently, there has been growing evidence of two growth regimes during the formation process with a significant portion of SEI-related capacity generated during the early stage.[57,93,94,104–106] For slow formation, the primary SEI is suspected to be *well-formed* where, by the end of formation, the system is saturated with degradation products, and the total lithium consumed by SEI production is similar across formation protocols.

To study this physical description of slow formation, we use cells from slow-formation conditions, consisting of 32 out of the 178 cells, for the physics-based investigation step. In a post-formation C/20 low-rate test (reference performance test [RPT]) across these cells, shown in Figure S12, the differential capacitance and d^2Q/dV^2 electrochemical signatures are nearly indistinguishable. This is an indication that the electrode utilization and remaining lithium inventory are likely similar across these cells. However, the performance, as quantified through cycle life, is not identical across all these cells. Specifically, the cells formed at the higher formation temperature tested at 55°C perform significantly better than the rest, perhaps indicating that the *quality* of formed degradation layers like SEI may be temperature dependent. The impact of the formation temperature on the electrochemical signature can be seen directly in the formation operating datasets, such as the dQ/dV and d^2Q/dV^2 curves in step B as shown in Figures 6A and 6B. These curves show little variation within cells formed at the same temperature but large variations across different formation temperatures. As the formation temperature decreases, a smoothing of both curves is observed, which makes

Table 6. MAPE and RMSE of each model at each outer fold and mean and HL estimator among five outer folds

		Agnostic (best)	AutoML (best)	Designed (best)
MAPE	outer fold 1	10.55	10.21	9.20*
	outer fold 2	11.06	8.14*	8.91
	outer fold 3	11.14	10.85	9.13*
	outer fold 4	11.35	9.72*	11.93
	outer fold 5	10.70	9.63*	10.05
	mean	10.96	9.71*	9.84
	HL	10.95	9.72	9.59*
RMSE	outer fold 1	108.79	120.44	98.98*
	outer fold 2	90.98	74.79*	88.51
	outer fold 3	124.81	136.92	97.33*
	outer fold 4	107.10	86.17*	108.54
	outer fold 5	100.82	83.14*	95.90
	mean	106.50	100.29	97.85*
	HL	107.10	101.79	97.44*

Asterisks indicate the smallest in each row, indicating the best performance.
[a]This small value was obtained by Weng et al.[44] having the cells from the same formation protocol in both their "validation" and "train/test" sets.
[b]From the same dataset being used for optimizing hyperparameters and evaluating the model performance.
[c]Each input data candidate was processed using interpolation at $p = 1{,}000$ uniformly distributed points along the input variable (x).
[d]HL estimator is the median of pairwise averages which is widely used to represent a distribution for its robustness.[91]

certain agnostic-model features visible through the electrochemical signatures.

To explain these trends, we use a surrogate model for the full-cell system, where the focus is on the temperature dependence of the electrochemical signatures during a simulation of step B. To achieve this goal, the underlying coupled transport and reaction dynamics for each electrode is simplified to a large ensemble of reactive particles in the model, where each particle has a rate-constant sampled from a defined distribution. The model can also be understood in the context of a distributed-resistance model, where many transport and reaction resistances are being lumped into the charge-transfer resistance, $R_{CT} = k_B T/ek_0$. The calculated current density in the underlying microscopic model for the i th particle in electrode j is modeled as

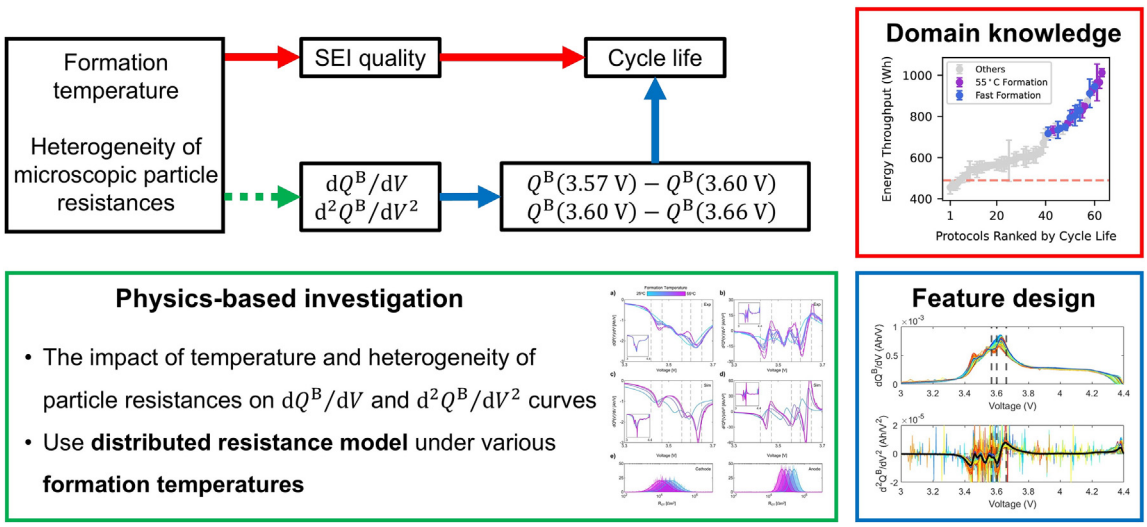

Figure 5. Schematics on how the systematic feature-design framework guides the physics-based investigation to find the physical meaning of the designed features

The red and blue arrows indicate the relationship learned from the domain knowledge and the feature-design work, respectively. The green dotted arrow indicates the missing link where the physics-based investigation is performed.

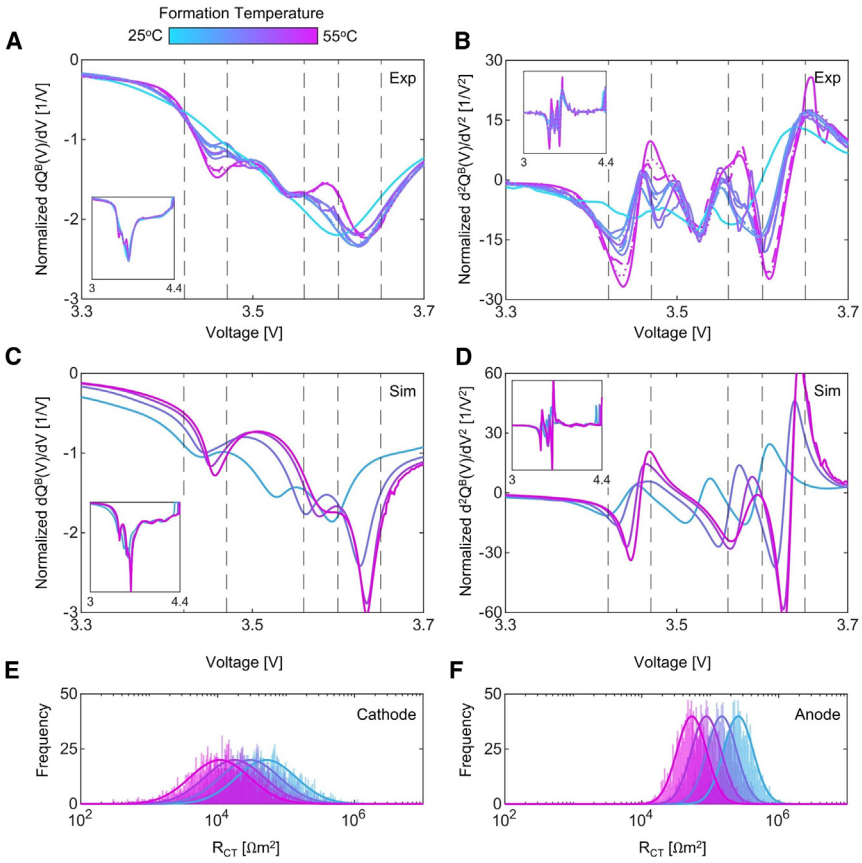

Figure 6. Physics-based investigation

(A and B) (A) Measured differential capacitance and (B) d^2Q/dV^2 for slow-formed cells across formation temperatures.

(C and D) (C) Reactive particle ensemble simulated differential capacitance and (D) d^2Q/dV^2 across formation temperatures.

(E and F) Simulated distribution of particle charge-transfer resistance across formation temperatures for (E) cathode and (F) anode, respectively. Both electrode reaction rates are governed by a singular log-Gaussian basis where at 298 K, the model is parameterized by $E_A = 45$ kJ/mol, $\bar{k}_{0,c} = 5\times10^{-7}$ A/m^{2}s, $\bar{k}_{0,a} = 10^{-7}$ A/m^{2}s, $\sigma_c = 1$, and $\sigma_a = 0.5$. Full model details can be found in Note S11.

$$j\left(\bar{c}_j^{(i)}, V, T\right) = k_{0,j}^{(i)} \exp\left(\frac{-E_A}{R}\left(\frac{1}{T} - \frac{1}{298}\right)\right) \times \left(1 - \bar{c}_j^{(i)}\right)\sqrt{\bar{c}_j^{(i)}}\sinh\left(-\frac{e\eta\left(\bar{c}_j^{(i)}, V_j\right)}{k_B T}\right), \quad \text{(Equation 6)}$$

based on the quantum theory of ion-coupled electron transfer (ICET).[107] The ICET rate expression has a symmetric Butler-Volmer dependence on overpotential (for equal reduction and oxidation ion-transfer energies) and an asymmetric dependence on electrode filling fraction, as recently confirmed by learning from X-ray images of battery nanoparticles.[108] The model also includes an Arrhenius temperature dependence in the pre-factor with an activation barrier, E_A (the activation enthalpy of ICET), which captures the effects of the formation-protocol temperature on the simulated dynamics. The full model formulation is described in Note S11.

By simulating the system with a log-Gaussian distribution for particle charge-transfer resistance at each electrode, characterized by a mean and standard deviation, we are able to simulate a set of step B curves across different temperatures with five free parameters. Comparing the simulated results in Figures 6C and 6D with the experimental dataset in Figures 6A and 6B, we see striking similarities in the location of the local maxima and minima in the d^2Q/dV^2 and their trends with temperature. These similarities allow us to theorize that the features contain information both on the average resistance of the two electrodes and the underlying resistance heterogeneity from the complex microscopic system state. While the former may be gleaned from simpler features, such as the differential resistance at a given SoC, the latter is unique to the designed features and could lead to the high performance observed. This underlying heterogeneity is likely a consequence of the quality of the SEI being formed, which is not obviously extractable from the formation-protocol parameters. In all, we hypothesize that the designed model performs better than the agnostic model because designed features not only encode some of the agnostic-model parameters, such as formation temperature, but also encode an underlying heterogeneity in the microscopic-particle resistances which varies from cell to cell and translates into the electrochemical signatures during formation.

Conclusions

The battery lifetime prediction community has long been trying to find an answer to the question: "how much data are needed to predict cycle life?" While the majority of the community focused on performing earlier cycle life prediction within the aging regime, our work presents how such prediction can be achieved by only using the formation data. Enabling extreme early cycle life prediction for untrained formation protocols, our work is expected to accelerate the optimization of the formation process. In this work, we develop a systematic feature-design framework to achieve extreme early cycle life prediction with minimal domain knowledge and user input. Using our framework, two simple $Q(V)$ features are designed from the last discharge step of the formation protocol. These features do not require additional diagnostic cycles, and they show good performance in comparing formation protocols across different temperatures, which is known to be the key parameter affecting the quality of

SEI layers. From the physics-based investigation guided by our feature-design framework, we attribute the predictiveness of the designed $Q(V)$ features to its ability to learn the impact of formation temperature and heterogeneity of microscopic-particle resistances on dQ/dV and d^2Q/dV^2 curves. As per the predictivity, robustness, and interpretability, the two designed features are suitable for evaluating the untrained formation protocol during the formation step.

While the main focus of this study was to perform extreme early cycle life prediction of untrained formation protocols for SC-NMC532/AG cells, industries may be interested in different cell chemistries, battery-performance metrics, and cycling conditions, depending on their applications. Not being tailored to any specific settings listed above, our framework is expected to design predictive features customized to each application. Interpretability of the designed features allows us to leverage the interplay between data-driven feature design and a mechanistic understanding of interested applications, providing the opportunity to further expand the domain knowledge of industrial formation processes. Besides optimizing the formation process, the same framework can be used to design features tailored for outlier detection during the manufacturing process when using the dataset consisting of cells under an identical formation protocol.

RESOURCE AVAILABILITY

Lead contact

Requests for further information and resources should be directed to and will be fulfilled by the lead contact, Richard D. Braatz (braatz@mit.edu).

Materials availability

This study did not generate new materials.

Data and code availability

The raw data used in this work, generated by Cui et al.,[47] can be found at https://data.matr.io/8/. The code and processed data used in this work have been deposited at Zenodo at https://doi.org/10.5281/zenodo.14916092 and are publicly available as of the date of publication.

ACKNOWLEDGMENTS

This work was supported by the Toyota Research Institute through D3BATT: Center for Data-Driven Design of Li-Ion Batteries. J.R. acknowledges support from the Kwanjeong Educational Foundation. The authors are grateful to Vivek Lam, Alexis Geslin, Justin Rose, Aki Takahashi, Huada Lian, Elia Arnese-Feffin, and Zhouhang (Amelia) Dai for providing comments.

AUTHOR CONTRIBUTIONS

Conceptualization, J.R., J.S., and R.D.B.; methodology, J.R., J.S., and R.D.B.; formal analysis, J.R., J.S., M.L.L., and X.C.; investigation, J.R., J.S., M.L.L., X.C., and R.D.B.; data curation, J.R. and X.C.; software, J.R., J.S., and M.L.L.; visualization, J.R. and M.L.L.; validation, J.R.; writing – original draft, J.R. and M.L.L.; writing – review and editing, J.R., J.S., M.L.L., X.C., W.C.C., M.Z.B., and R.D.B.; supervision, W.C.C., M.Z.B., and R.D.B.; funding acquisition, W.C.C., M.Z.B., and R.D.B.

DECLARATION OF INTERESTS

The authors declare no competing interests.

SUPPLEMENTAL INFORMATION

Supplemental information can be found online at https://doi.org/10.1016/j.joule.2025.101884.

Received: October 8, 2024
Revised: January 14, 2025
Accepted: February 28, 2025
Published: March 28, 2025

REFERENCES

1. Bandhauer, T.M., Garimella, S., and Fuller, T.F. (2011). A critical review of thermal issues in lithium-ion batteries. J. Electrochem. Soc. *158*, R1–R25. https://doi.org/10.1149/1.3515880.
2. Deng, D. (2015). Li-ion batteries: basics, progress, and challenges. Energy Sci. Eng. *3*, 385–418. https://doi.org/10.1002/ese3.95.
3. Deng, J., Bae, C., Marcicki, J., Masias, A., and Miller, T. (2018). Safety modelling and testing of lithium-ion batteries in electrified vehicles. Nat. Energy *3*, 261–266. https://doi.org/10.1038/s41560-018-0122-3.
4. Attia, P.M., Grover, A., Jin, N., Severson, K.A., Markov, T.M., Liao, Y.-H., Chen, M.H., Cheong, B., Perkins, N., Yang, Z., et al. (2020). Closed-loop optimization of fast-charging protocols for batteries with machine learning. Nature *578*, 397–402. https://doi.org/10.1038/s41586-020-1994-5.
5. Davies, G., Knehr, K.W., Van Tassell, B., Hodson, T., Biswas, S., Hsieh, A.G., and Steingart, D.A. (2017). State of charge and state of health estimation using electrochemical acoustic time of flight analysis. J. Electrochem. Soc. *164*, A2746–A2755. https://doi.org/10.1149/2.1411712jes.
6. Severson, K.A., Attia, P.M., Jin, N., Perkins, N., Jiang, B., Yang, Z., Chen, M.H., Aykol, M., Herring, P.K., Fraggedakis, D., et al. (2019). Data-driven prediction of battery cycle life before capacity degradation. Nat. Energy *4*, 383–391. https://doi.org/10.1038/s41560-019-0356-8.
7. Sulzer, V., Mohtat, P., Lee, S., Siegel, J.B., and Stefanopoulou, A.G. (2021). Promise and challenges of a data-driven approach for battery lifetime prognostics. In American Control Conference (ACC), pp. 4427–4433. https://doi.org/10.23919/ACC50511.2021.9483312.
8. Zhang, K., Yin, J., and He, Y. (2021). Acoustic emission detection and analysis method for health status of lithium ion batteries. Sensors (Basel) *21*, 712. https://doi.org/10.3390/s21030712.
9. Greenbank, S., and Howey, D. (2022). Automated feature extraction and selection for data-driven models of rapid battery capacity fade and end of life. IEEE Trans. Ind. Inform. *18*, 2965–2973. https://doi.org/10.1109/TII.2021.3106593.
10. Jones, P.K., Stimming, U., and Lee, A.A. (2022). Impedance-based forecasting of lithium-ion battery performance amid uneven usage. Nat. Commun. *13*, 4806. https://doi.org/10.1038/s41467-022-32422-w.
11. Paulson, N.H., Kubal, J., Ward, L., Saxena, S., Lu, W., and Babinec, S.J. (2022). Feature engineering for machine learning enabled early prediction of battery lifetime. J. Power Sources *527*, 231127. https://doi.org/10.1016/j.jpowsour.2022.231127.
12. Schaeffer, J., Galuppini, G., Rhyu, J., Asinger, P.A., Droop, R., Findeisen, R., and Braatz, R.D. (2024). Cycle life prediction for lithium-ion batteries: Machine learning and more. In American Control Conference (ACC), pp. 763–768. https://doi.org/10.23919/ACC60939.2024.10644790.
13. Schaeffer, J., Lenz, E., Chueh, W.C., Bazant, M.Z., Findeisen, R., and Braatz, R.D. (2024). Interpretation of high-dimensional linear regression: Effects of nullspace and regularization demonstrated on battery data. Comput. Chem. Eng. *180*, 108471. https://doi.org/10.1016/j.compchemeng.2023.108471.
14. Ning, G., and Popov, B.N. (2004). Cycle life modeling of lithium-ion batteries. J. Electrochem. Soc. *151*, A1584–A1591. https://doi.org/10.1149/1.1787631.
15. Deshpande, R., Verbrugge, M., Cheng, Y.-T., Wang, J., and Liu, P. (2012). Battery cycle life prediction with coupled chemical degradation and

fatigue mechanics. J. Electrochem. Soc. *159*, A1730–A1738. https://doi.org/10.1149/2.049210jes.

16. Reniers, J.M., Mulder, G., and Howey, D.A. (2019). Review and performance comparison of mechanical-chemical degradation models for lithium-ion batteries. J. Electrochem. Soc. *166*, A3189–A3200. https://doi.org/10.1149/2.0281914jes.
17. Downey, A., Lui, Y.-H., Hu, C., Laflamme, S., and Hu, S. (2019). Physics-based prognostics of lithium-ion battery using non-linear least squares with dynamic bounds. Reliab. Eng. Syst. Saf. *182*, 1–12. https://doi.org/10.1016/j.ress.2018.09.018.
18. El-Dalahmeh, M., Al-Greer, M., El-Dalahmeh, M., and Bashir, I. (2023). Physics-based model informed smooth particle filter for remaining useful life prediction of lithium-ion battery. Measurement *214*, 112838. https://doi.org/10.1016/j.measurement.2023.112838.
19. Liu, J., Wang, W., Ma, F., Yang, Y.B., and Yang, C.S. (2012). A data-model-fusion prognostic framework for dynamic system state forecasting. Eng. Appl. Artif. Intell. *25*, 814–823. https://doi.org/10.1016/j.engappai.2012.02.015.
20. Liao, L., and Kottig, F. (2014). Review of hybrid prognostics approaches for remaining useful life prediction of engineered systems, and an application to battery life prediction. IEEE Trans. Reliab. *63*, 191–207. https://doi.org/10.1109/TR.2014.2299152.
21. Zheng, X., and Fang, H. (2015). An integrated unscented Kalman filter and relevance vector regression approach for lithium-ion battery remaining useful life and short-term capacity prediction. Reliab. Eng. Syst. Saf. *144*, 74–82. https://doi.org/10.1016/j.ress.2015.07.013.
22. Chang, Y., Fang, H., and Zhang, Y. (2017). A new hybrid method for the prediction of the remaining useful life of a lithium-ion battery. Appl. Energy *206*, 1564–1578. https://doi.org/10.1016/j.apenergy.2017.09.106.
23. Aitio, A., and Howey, D. (2020). Combining non-parametric and parametric models for stable and computationally efficient battery health estimation. In ASME 2020 Dynamic Systems and Control Conference, pp. V001T20A002. https://doi.org/10.1115/DSCC2020-3180.
24. Sulzer, V., Mohtat, P., Aitio, A., Lee, S., Yeh, Y.T., Steinbacher, F., Khan, M.U., Lee, J.W., Siegel, J.B., Stefanopoulou, A.G., et al. (2021). The challenge and opportunity of battery lifetime prediction from field data. Joule *5*, 1934–1955. https://doi.org/10.1016/j.joule.2021.06.005.
25. Aykol, M., Gopal, C.B., Anapolsky, A., Herring, P.K., van Vlijmen, B., Berliner, M.D., Bazant, M.Z., Braatz, R.D., Chueh, W.C., and Storey, B.D. (2021). Perspective—Combining physics and machine learning to predict battery lifetime. J. Electrochem. Soc. *168*, 030525. https://doi.org/10.1149/1945-7111/abec55.
26. Schaeffer, J., Lenz, E., Gulla, D., Bazant, M.Z., Braatz, R.D., and Findeisen, R. (2024). Gaussian process-based online health monitoring and fault analysis of lithium-ion battery systems from field data. Cell Rep. Phy. Sci. *5*, 102258. https://doi.org/10.1016/j.xcrp.2024.102258.
27. Bloom, I., Jansen, A.N., Abraham, D.P., Knuth, J., Jones, S.A., Battaglia, V.S., and Henriksen, G.L. (2005). Differential voltage analyses of high-power, lithium-ion cells. J. Power Sources *139*, 295–303. https://doi.org/10.1016/j.jpowsour.2004.07.021.
28. Dahn, H.M., Smith, A.J., Burns, J.C., Stevens, D.A., and Dahn, J.R. (2012). User-friendly differential voltage analysis freeware for the analysis of degradation mechanisms in Li-ion batteries. J. Electrochem. Soc. *159*, A1405–A1409. https://doi.org/10.1149/2.013209jes.
29. Weng, A., Siegel, J.B., and Stefanopoulou, A. (2023). Differential voltage analysis for battery manufacturing process control. Front. Energy Res. *11*, 1087269. https://doi.org/10.3389/fenrg.2023.1087269.
30. Lin, J., and Khoo, E. (2024). Identifiability study of lithium-ion battery capacity fade using degradation mode sensitivity for a minimally and intuitively parametrized electrode-specific cell open-circuit voltage model. J. Power Sources *605*, 234446. https://doi.org/10.1016/j.jpowsour.2024.234446.
31. Dubarry, M., Truchot, C., and Liaw, B.Y. (2012). Synthesize battery degradation modes via a diagnostic and prognostic model. J. Power Sources *219*, 204–216. https://doi.org/10.1016/j.jpowsour.2012.07.016.
32. Dubarry, M., and Anseán, D. (2022). Best practices for incremental capacity analysis. Front. Energy Res. *10*, 1023555. https://doi.org/10.3389/fenrg.2022.1023555.
33. Huang, Q.-A., Hui, R., Wang, B., and Zhang, J. (2007). A review of AC impedance modeling and validation in SOFC diagnosis. Electrochim. Acta *52*, 8144–8164. https://doi.org/10.1016/j.electacta.2007.05.071.
34. Chang, B.-Y., and Park, S.-M. (2010). Electrochemical impedance spectroscopy. Annu. Rev. Anal. Chem. (Palo Alto Calif) *3*, 207–229. https://doi.org/10.1146/annurev.anchem.012809.102211.
35. Schaeffer, J., Gasper, P., Garcia-Tamayo, E., Gasper, R., Adachi, M., Pablo Gaviria-Cardona, J.P.G., Montoya-Bedoya, S., Bhutani, A., Schiek, A., Goodall, R., et al. (2023). Machine learning benchmarks for the classification of equivalent circuit models from electrochemical impedance spectra. J. Electrochem. Soc. *170*, 060512. https://doi.org/10.1149/1945-7111/acd8fb.
36. Dees, D., Gunen, E., Abraham, D., Jansen, A., and Prakash, J. (2008). Electrochemical modeling of lithium-ion positive electrodes during hybrid pulse power characterization tests. J. Electrochem. Soc. *155*, A603–A613. https://doi.org/10.1149/1.2939211.
37. Holland, C.E., Weidner, J.W., Dougal, R.A., and White, R.E. (2002). Experimental characterization of hybrid power systems under pulse current loads. J. Power Sources *109*, 32–37. https://doi.org/10.1016/S0378-7753(02)00044-7.
38. Che, Y., Vilsen, S.B., Meng, J., Sui, X., and Teodorescu, R. (2023). Battery health prognostic with sensor-free differential temperature voltammetry reconstruction and capacity estimation based on multi-domain adaptation. eTransportation *17*, 100245. https://doi.org/10.1016/j.etran.2023.100245.
39. Huang, S.-C., Tseng, K.-H., Liang, J.-W., Chang, C.-L., and Pecht, M. (2017). An online SOC and SOH estimation model for lithium-ion batteries. Energies *10*, 512. https://doi.org/10.3390/en10040512.
40. Tian, J., Xiong, R., and Shen, W. (2020). State-of-health estimation based on differential temperature for lithium ion batteries. IEEE Trans. Power Electron. *35*, 10363–10373. https://doi.org/10.1109/TPEL.2020.2978493.
41. Son, S., Jeong, S., Kwak, E., Kim, J.-h., and Oh, K.-Y. (2022). Integrated framework for SOH estimation of lithium-ion batteries using multiphysics features. Energy *238*, 121712. https://doi.org/10.1016/j.energy.2021.121712.
42. Sun, J., and Kainz, J. (2023). Optimization of hybrid pulse power characterization profile for equivalent circuit model parameter identification of Li-ion battery based on Taguchi method. J. Energy Storage *70*, 108034. https://doi.org/10.1016/j.est.2023.108034.
43. Rhyu, J., Zhuang, D., Bazant, M.Z., and Braatz, R.D. (2024). Optimum model-based design of diagnostics experiments (DOE) with hybrid pulse power characterization (HPPC) for lithium-ion batteries. J. Electrochem. Soc. *171*, 070544. https://doi.org/10.1149/1945-7111/ad63ce.
44. Weng, A., Mohtat, P., Attia, P.M., Sulzer, V., Lee, S., Less, G., and Stefanopoulou, A. (2021). Predicting the impact of formation protocols on battery lifetime immediately after manufacturing. Joule *5*, 2971–2992. https://doi.org/10.1016/j.joule.2021.09.015.
45. Wood, D.L., Li, J., and An, S.J. (2019). Formation challenges of lithium-ion battery manufacturing. Joule *3*, 2884–2888. https://doi.org/10.1016/j.joule.2019.11.002.
46. An, S.J., Li, J., Du, Z., Daniel, C., and Wood, D.L. (2017). Fast formation cycling for lithium ion batteries. J. Power Sources *342*, 846–852. https://doi.org/10.1016/j.jpowsour.2017.01.011.
47. Cui, X., Kang, S.D., Wang, S., Rose, J.A., Lian, H., Geslin, A., Torrisi, S.B., Bazant, M.Z., Sun, S., and Chueh, W.C. (2024). Data-driven analysis of

battery formation reveals the role of electrode utilization in extending cycle life. Joule *8*, 3072–3087. https://doi.org/10.1016/j.joule.2024.07.024.

48. Liu, Y., Zhang, R., Wang, J., and Wang, Y. (2021). Current and future lithium-ion battery manufacturing. iScience *24*, 102332. https://doi.org/10.1016/j.isci.2021.102332.
49. This small value was obtained by Weng et al.[44] having the cells from the same formation protocol in both their "validation" set and "train/test" sets.
50. Schranzhofer, H., Bugajski, J., Santner, H.J., Korepp, C., Möller, K.-C., Besenhard, J.O., Winter, M., and Sitte, W. (2006). Electrochemical impedance spectroscopy study of the SEI formation on graphite and metal electrodes. J. Power Sources *153*, 391–395. https://doi.org/10.1016/j.jpowsour.2005.05.034.
51. Zhang, Y., Tang, Q., Zhang, Y., Wang, J., Stimming, U., and Lee, A.A. (2020). Identifying degradation patterns of lithium ion batteries from impedance spectroscopy using machine learning. Nat. Commun. *11*, 1706. https://doi.org/10.1038/s41467-020-15235-7.
52. Pietsch, P., and Wood, V. (2017). X-ray tomography for lithium ion battery research: A practical guide. Annu. Rev. Mater. Res. *47*, 451–479. https://doi.org/10.1146/annurev-matsci-070616-123957.
53. Wood, V. (2018). X-ray tomography for battery research and development. Nat. Rev. Mater. *3*, 293–295. https://doi.org/10.1038/s41578-018-0053-4.
54. Condon, A., Buscarino, B., Moch, E., Sehnert, W.J., Miles, O., Herring, P.K., and Attia, P.M. (2024). A dataset of over one thousand computed tomography scans of battery cells. Data Brief *55*, 110614. https://doi.org/10.1016/j.dib.2024.110614.
55. Hsieh, A.G., Bhadra, S., Hertzberg, B.J., Gjeltema, P.J., Goy, A., Fleischer, J.W., and Steingart, D.A. (2015). Electrochemical-acoustic time of flight: in operando correlation of physical dynamics with battery charge and health. Energy Environ. Sci. *8*, 1569–1577. https://doi.org/10.1039/C5EE00111K.
56. Ke, Q., Jiang, S., Li, W., Lin, W., Li, X., and Huang, H. (2022). Potential of ultrasonic time-of-flight and amplitude as the measurement for state of charge and physical changings of lithium-ion batteries. J. Power Sources *549*, 232031. https://doi.org/10.1016/j.jpowsour.2022.232031.
57. Weng, A., Olide, E., Kovalchuk, I., Siegel, J.B., and Stefanopoulou, A. (2023). Modeling battery formation: Boosted SEI growth, multi-species reactions, and irreversible expansion. J. Electrochem. Soc. *170*, 090523. https://doi.org/10.1149/1945-7111/aceffe.
58. Stein, M. (1987). Large sample properties of simulations using Latin hypercube sampling. Technometrics *29*, 143–151. https://doi.org/10.1080/00401706.1987.10488205.
59. Kapoor, S., and Narayanan, A. (2023). Leakage and the reproducibility crisis in machine-learning-based science. Patterns *4*, 100804. https://doi.org/10.1016/j.patter.2023.100804.
60. Gibney, E. (2022). Could machine learning fuel a reproducibility crisis in science? Nature *608*, 250–251. https://doi.org/10.1038/d41586-022-02035-w.
61. Geslin, A., van Vlijmen, B., Cui, X., Bhargava, A., Asinger, P.A., Braatz, R.D., and Chueh, W.C. (2023). Selecting the appropriate features in battery lifetime predictions. Joule *7*, 1956–1965. https://doi.org/10.1016/j.joule.2023.07.021.
62. From the same dataset being used for optimizing hyperparameters and evaluating the model performance.
63. Sun, W., and Braatz, R.D. (2021). Smart process analytics for predictive modeling. Comput. Chem. Eng. *144*, 107134. https://doi.org/10.1016/j.compchemeng.2020.107134.
64. Hoerl, A.E., and Kennard, R.W. (1970). Ridge regression: Biased estimation for nonorthogonal problems. Technometrics *12*, 55–67. https://doi.org/10.1080/00401706.1970.10488634.
65. Zou, H., and Hastie, T. (2005). Regularization and variable selection via the elastic net. J. R. Stat. Soc. B *67*, 301–320. https://doi.org/10.1111/j.1467-9868.2005.00503.x.
66. Geladi, P., and Kowalski, B.R. (1986). Partial least-squares regression: a tutorial. Anal. Chim. Acta *185*, 1–17. https://doi.org/10.1016/0003-2670(86)80028-9.
67. Chun, H., and Keleş, S. (2010). Sparse partial least squares regression for simultaneous dimension reduction and variable selection. J. R. Stat. Soc. Series B Stat. Methodol. *72*, 3–25. https://doi.org/10.1111/j.1467-9868.2009.00723.x.
68. Breiman, L. (2001). Random forests. Mach. Learn. *45*, 5–32. https://doi.org/10.1023/A:1010933404324.
69. Vapnik, V.N. (2000). The Nature of Statistical Learning Theory (Springer). https://doi.org/10.1007/978-1-4757-3264-1.
70. Chen, T., and Guestrin, C. (2016). XGBoost: A scalable tree boosting system. In Proceedings of the 22nd ACM SIGKDD International Conference on Knowledge Discovery and Data Mining (ACM), pp. 785–794. https://doi.org/10.1145/2939672.2939785.
71. Sun, W., and Braatz, R.D. (2020). ALVEN: Algebraic learning via elastic net for static and dynamic nonlinear model identification. Comput. Chem. Eng. *143*, 107103. https://doi.org/10.1016/j.compchemeng.2020.107103.
72. Seber, P., and Braatz, R.D. (2024). LCEN: A novel feature selection algorithm for nonlinear, interpretable machine learning models. Preprint at arXiv. https://doi.org/10.48550/arXiv.2402.17120.
73. Lundberg, S.M., and Lee, S.-I. (2017). A unified approach to interpreting model predictions. In Proceedings of the 31st International Conference on Neural Information Processing Systems, pp. 4768–4777. https://doi.org/10.5555/3295222.3295230.
74. Each input data candidate was processed using interpolation at p = 1,000 uniformly distributed points along the input variable (x).
75. He, X., Zhao, K., and Chu, X. (2021). AutoML: A survey of the state-of-the-art. Knowl. Based Syst. *212*, 106622. https://doi.org/10.1016/j.knosys.2020.106622.
76. Christ, M., Braun, N., Neuffer, J., and Kempa-Liehr, A.W. (2018). Time Series FeatuRe Extraction on basis of Scalable Hypothesis tests (tsfresh – A Python package). Neurocomputing *307*, 72–77. https://doi.org/10.1016/j.neucom.2018.03.067.
77. Brighente, A., Conti, M., Donadel, D., and Turrin, F. (2024). EVScout2.0: Electric Vehicle Profiling through Charging Profile. ACM Trans. Cyber Phys. Syst. *8*, 1–24. https://doi.org/10.1145/3565268.
78. Wang, R., Li, J., Wang, X., Wang, S., and Pecht, M. (2024). Deep learning model for state of health estimation of lithium batteries based on relaxation voltage. J. Energy Storage *79*, 110189. https://doi.org/10.1016/j.est.2023.110189.
79. Wang, C., Baratchi, M., Bäck, T., Hoos, H.H., Limmer, S., and Olhofer, M. (2022). Towards time-series feature engineering in automated machine learning for multi-step-ahead forecasting. Eng. Proc. *18*, 17. https://doi.org/10.3390/engproc2022018017.
80. Zhang, W., Dong, X., Li, H., Xu, J., and Wang, D. (2020). Unsupervised detection of abnormal electricity consumption behavior based on feature engineering. IEEE Access *8*, 55483–55500. https://doi.org/10.1109/ACCESS.2020.2980079.
81. Liu, G., Li, L., Zhang, L., Li, Q., and Law, S.S. (2020). Sensor faults classification for SHM systems using deep learning-based method with Tsfresh features. Smart Mater. Struct. *29*, 075005. https://doi.org/10.1088/1361-665X/ab85a6.
82. Schaeffer, J., Rhyu, J., Droop, R., Findeisen, R., and Braatz, R. (2024). Interpretation of high-dimensional regression coefficients by comparison with linearized compressing features. Preprint at arXiv. https://doi.org/10.48550/arXiv.2411.12060.
83. Schaeffer, J., and Braatz, R.D. (2022). Latent Variable Method Demonstrator — software for understanding multivariate data analytics

algorithms. Comput. Chem. Eng. *167*, 108014. https://doi.org/10.1016/j.compchemeng.2022.108014.

84. Tibshirani, R.J., and Taylor, J. (2011). The solution path of the generalized lasso. Ann. Statist. *39*, 1335–1371. https://doi.org/10.1214/11-AOS878.
85. Müller, M. (2007). Information Retrieval for Music and Motion (Springer).
86. Wang, K., and Gasser, T. (1997). Alignment of curves by dynamic time warping. Ann. Statist. *25*, 1251–1276. https://doi.org/10.1214/aos/1069362747.
87. Mei, K., Tan, M., Yang, Z., and Shi, S. (2022). Modeling of feature selection based on random forest algorithm and Pearson correlation coefficient. J. Phys. Conf. Ser. *2219*, 012046. https://doi.org/10.1088/1742-6596/2219/1/012046.
88. A.E. Hassanien, ed. (2019). Machine Learning Paradigms: Theory and Application (Springer).
89. Liu, Y., Mu, Y., Chen, K., Li, Y., and Guo, J. (2020). Daily activity feature selection in smart homes based on Pearson correlation coefficient. Neural Process. Lett. *51*, 1771–1787. https://doi.org/10.1007/s11063-019-10185-8.
90. HL estimator is the median of pairwise averages which is widely used to represent a distribution for its robustness.[91]
91. Hodges, J.L., Jr., and Lehmann, E.L. (1963). Estimates of location based on rank tests. Ann. Math. Statist. *34*, 598–611. https://doi.org/10.1214/aoms/1177704172.
92. Pinson, M.B., and Bazant, M.Z. (2013). Theory of SEI formation in rechargeable batteries: Capacity fade, accelerated aging and lifetime prediction. J. Electrochem. Soc. *160*, A243–A250. https://doi.org/10.1149/2.044302jes.
93. Attia, P.M., Das, S., Harris, S.J., Bazant, M.Z., and Chueh, W.C. (2019). Electrochemical kinetics of SEI growth on carbon black: Part I. Experiments. J. Electrochem. Soc. *166*, E97–E106. https://doi.org/10.1149/2.0231904jes.
94. Das, S., Attia, P.M., Chueh, W.C., and Bazant, M.Z. (2019). Electrochemical kinetics of SEI growth on carbon black: Part II. Modeling. J. Electrochem. Soc. *166*, E107–E118. https://doi.org/10.1149/2.0241904jes.
95. Peled, E., Golodnttsky, D., Ardel, G., Menachem, C., Bar Tow, D., and Eshkenazy, V. (1995). The role of SEI in lithium and lithium ion batteries. MRS Proc. *393*, 209. https://doi.org/10.1557/PROC-393-209.
96. Ploehn, H.J., Ramadass, P., and White, R.E. (2004). Solvent diffusion model for aging of lithium-ion battery cells. J. Electrochem. Soc. *151*, A456–A462. https://doi.org/10.1149/1.1644601.
97. Ramadass, P., Haran, B., Gomadam, P.M., White, R., and Popov, B.N. (2004). Development of first principles capacity fade model for Li-ion cells. J. Electrochem. Soc. *151*, A196–A203. https://doi.org/10.1149/1.1634273.
98. Smith, A.J., Burns, J.C., Zhao, X., Xiong, D., and Dahn, J.R. (2011). A high precision coulometry study of the SEI growth in Li/graphite cells. J. Electrochem. Soc. *158*, A447–A452. https://doi.org/10.1149/1.3557892.
99. Peled, E., and Menkin, S. (2017). Review—SEI: past, present and future. J. Electrochem. Soc. *164*, A1703–A1719. https://doi.org/10.1149/2.1441707jes.
100. An, S.J., Li, J., Daniel, C., Mohanty, D., Nagpure, S., and Wood, D.L. (2016). The state of understanding of the lithium-ion-battery graphite solid electrolyte interphase (SEI) and its relationship to formation cycling. Carbon *105*, 52–76. https://doi.org/10.1016/j.carbon.2016.04.008.
101. Thevenin, J.G., and Muller, R.H. (1987). Impedance of lithium electrodes in a propylene carbonate electrolyte. J. Electrochem. Soc. *134*, 273–280. https://doi.org/10.1149/1.2100445.
102. Aurbach, D., Weissman, I., Zaban, A., and Chusid, O. (1994). Correlation between surface chemistry, morphology, cycling efficiency and interfacial properties of Li electrodes in solutions containing different Li salts. Electrochim. Acta *39*, 51–71. https://doi.org/10.1016/0013-4686(94)85010-0.
103. Peled, E., Bar Tow, D., Merson, A., Gladkich, A., Burstein, L., and Golodnitsky, D. (2001). Composition, depth profiles and lateral distribution of materials in the SEI built on HOPG-TOF SIMS and XPS studies. J. Power Sources *97–98*, 52–57. https://doi.org/10.1016/S0378-7753(01)00505-5.
104. Huang, W., Attia, P.M., Wang, H., Renfrew, S.E., Jin, N., Das, S., Zhang, Z., Boyle, D.T., Li, Y., Bazant, M.Z., et al. (2019). Evolution of the solid–electrolyte interphase on carbonaceous anodes visualized by atomic-resolution cryogenic electron microscopy. Nano Lett. *19*, 5140–5148. https://doi.org/10.1021/acs.nanolett.9b01515.
105. Thaman, H., Li, M., Rose, J., Narasimhan, S., Xu, X., Yeh, C.-n., Jin, N., Akbashev, A., Davidoff, I., Bazant, M.Z., et al. (2024). Two-Stage Growth of Solid Electrolyte Interphase on Copper: Imaging and Quantification by Operando Atomic Force Microscopy. Preprint at ChemRxiv. https://doi.org/10.26434/chemrxiv-2024-nhh8k.
106. Von Kolzenberg, L., Latz, A., and Horstmann, B. (2020). Solid–electrolyte interphase during battery cycling: Theory of growth regimes. ChemSusChem *13*, 3901–3910. https://doi.org/10.1002/cssc.202000867.
107. Bazant, M.Z. (2023). Unified quantum theory of electrochemical kinetics by coupled ion–electron transfer. Faraday Discuss. *246*, 60–124. https://doi.org/10.1039/D3FD00108C.
108. Zhao, H., Deng, H.D., Cohen, A.E., Lim, J., Li, Y., Fraggedakis, D., Jiang, B., Storey, B.D., Chueh, W.C., Braatz, R.D., et al. (2023). Learning heterogeneous reaction kinetics from X-ray videos pixel by pixel. Nature *621*, 289–294. https://doi.org/10.1038/s41586-023-06393-x.